Green Chemistry

# Solvent-Induced Membrane Stress in Biofuel Production: Molecular Insights from Small-Angle Scattering and All-Atom Molecular Dynamics Simulations



| | |
|---|---|
| Journal: | *Green Chemistry* |
| Manuscript ID | GC-ART-06-2020-001865.R1 |
| Article Type: | Paper |
| Date Submitted by the Author: | 06-Aug-2020 |





| | |
|---|---|
| Complete List of Authors: | Smith, Micholas; UT/ORNL Center for Molecular Biophysics; The University of Tennessee Knoxville, Biochemistry, Cellular & Molecular Biology<br>Pingali, Sai Venkatesh; Oak Ridge National Laboratory, Biology and Soft Matter Division<br>Elkins, James G.; Oak Ridge Natl Lab,<br>Bolmatov, Dima; Oak Ridge National Laboratory<br>Standaert, Robert; East Tennessee State University, Chemistry<br>Nickels, Jonathan; University of Cincinnati, CEAS - Chemical & Env Eng<br>Urban, Volker; Oak Ridge National Laboratory, Neutron Scattering Division<br>Katsaras, John; Oak Ridge National Laboratory, Neutron Sciences Directorate<br>Davison, Brian; Oak Ridge National Laboratory, Biosciences Division<br>Smith, Jeremy; Oak Ridge National Laboratory, UT/ORNL Center for Molecular Biophysics<br>Petridis, Loukas; Oak Ridge National Laboratory, Center for Molecular Biophyscis |
| | |

# Solvent-Induced Membrane Stress in Biofuel Production: Molecular Insights from Small-Angle Scattering and All-Atom Molecular Dynamics Simulations

Micholas Dean Smith[1,2], Sai Venkatesh Pingali[3], James G. Elkins[3], Dima Bolmatov[3], Robert F. Standaert[3, 4], Jonathan D. Nickels[5], Volker S. Urban[3], John Katsaras[3,6,7], Brian Davison[3], Jeremy C. Smith[1,2*], & Loukas Petridis[1,2 *]

* Corresponding authors: smithjc@ornl.gov & petridisl@ornl.gov

[1] Center for Molecular Biophysics, University of Tennessee/Oak Ridge National Laboratory, Oak Ridge National Laboratory, PO Box 2008, Oak Ridge, TN 37831

[2] Department of Biochemistry and Cellular and Molecular Biology, University of Tennessee, M407 Walters Life Sciences, 1414 Cumberland Avenue, Knoxville, TN 37996

[3] Oak Ridge National Laboratory, PO Box 2008, Oak Ridge, TN 37831

[4] Department of Chemistry, East Tennessee State University, PO Box: 70695, Johnson City, TN 37614

[5]Department of Chemical and Environmental Engineering, University of Cincinnati, 2600 Clifton Ave. Cincinnati, OH 45220

[6]Department of Physics and Astronomy, 401 Nielsen Physics Building, 1408 Circle Drive, Knoxville, TN 37996

[7]Shull Wollan Center, Oak Ridge National Laboratory, Oak Ridge, TN 37831

**Abstract**

The disruptive effect of organic solvents on microbial membranes represents a significant challenge to the economical production of green fuels and value-added chemicals from lignocellulosic feedstocks. One route to overcoming this challenge is to engineer microbes with membranes capable of resisting organic solvent stresses. In this regard, it is useful to understand the mechanisms by which organic solvents disrupt typical biomembranes. Here, molecular dynamics (MD) simulation, complemented by small-angle X-ray and neutron scattering (SANS/SAXS), provide a molecular-scale view of the disruption of a microbial model membrane by 1-butanol and tetrahydrofuran (THF), two common water-organic cosolvent mixtures of importance in biofuel production. Solvent interactions at the interface between the head-group and fatty acid tail regions lead to more dramatic membrane changes than interactions solely at the head-groups or tails. Although both organic solvents are found to partition into the membrane, the depth of solvent penetration into the membrane is quite different. Specifically, 1-butanol localizes near the interface between the lipid heads and tails at low concentrations, but partitions into both the head and tail regions at high concentrations. In contrast, THF, overall, partitions less than 1-butanol and prefers the lipid tail regions. Importantly, the presence of 1-butanol near the head/tail interface introduces drastic membrane changes not seen with THF. The organic solvent interactions with the lipids lead to membrane thinning and fluidization, but more so for 1-butanol than for THF. These results suggest that an aim for the future engineering of robust membranes could be to design lipid head groups that reduce the accumulation of organic solvents at the head-tail interface and that rational designs need also be cognizant of the different solvent-specific mechanisms responsible for membrane disruption.

**Introduction**

Biofuel production from lignocellulosic biomass requires two critical steps: (i) plant cell wall deconstruction to sugars (*via* pretreatment and hydrolysis) and (ii) biological upgrading of sugars to fuels (*via* microbial fermentation). Historically, the former task has been considered the largest road-block to the economic development of biofuels from lignocellulosic biomass (a complex material consisting mostly of cellulose fibrils, polyphenolic lignin, and heterogeneous polysaccharides)[1-6] as the material is highly resistant to breakdown, which limits the release of sugars for upgrading[7, 8]. Recent advances, however, in the use of aqueous-organic cosolvent lignocellulosic pretreatment technologies, such as the use of mixtures of water and tetrahydrofuran (THF), have been found to disrupt many of the stabilizing interactions within the lignocellulose matrix and have led to significantly increased sugar accessibility and release[1, 9-19]. Furthermore, these pretreatments may solubilize and fractionate lignin for downstream conversion into valuable non-fuel platform chemicals[13, 18, 20].

With the increased efficiency of these new cosolvent-based pretreatments, the challenge to economically produce lignocellulosic-derived biofuels and bioproducts will inevitably shift away from the historic challenge of overcoming plant recalcitrance and will instead focus on improving biological upgrading strategies (bio-upgrading). Indeed, it has become clear that to improve bio-upgrading, one needs to develop microbes capable of producing and tolerating non-ethanol biofuels at higher product titers[21, 22]. Industrial solvents and their chaotropic effects on various cellular targets are known to impact growth and fermentation in several relevant biofuel-producing microbes[23, 24]. One prominent cause, for example, of abiotic stress with regards to biofuel production is aliphatic alcohols, which are both fermentation products and potent inhibitors. In the case of butanol fermentation, high-titers ( > 30 g/L) cannot be achieved *in situ* due to the toxicity of the end product[25, 26]. Abiotic stresses also arise from residual pretreatment solvents that inhibit fermentation after lignocellulose pretreatment[27-29].

Several mechanisms may be responsible for the solvent cytotoxicity that leads to limited fermentation. The mechanism upon which we focus here is membrane disruption by solvents, which can act as chaotropic agents causing disorder in membrane assemblies[23, 24]. Identifying these stresses has

motivated efforts aimed at improving microbial robustness by manipulating microbial biomembranes to withstand solvent stress[30]. Prior attempts to use iterative directed evolution approaches to increase membrane robustness have thus far proven ineffective, with increases in butanol resistance being achieved at the cost of inhibited cellular growth[30]. Despite decades of research[28-34], microbes capable of producing and tolerating non-ethanol biofuel product titers remain elusive.

An alternative approach is to rationally improve microbial membrane robustness based on understanding the molecular details of solvent-induced membrane stress. Such an approach may prove to be fruitful, as biological membranes serve crucial roles as selective barriers, reaction sites, and communication hubs[35-38]. In order to perform these many functions, the fluidity and structure of membranes are carefully controlled to prevent their disruption due to external stressors,[39-44] – albeit at a great energetic cost to the cell. Lessons learned from the physical understanding of model membranes under stress[45-53] can thus aid in guiding the rational design of robust membranes.

Here, we report the results of a joint molecular-dynamics (MD)/small-angle scattering (SAS) study on the influence of two common biofuel-relevant solvents, namely 1-butanol (referred to as butanol for the remainder of this text) and THF, on a simplified model microbial membrane composed of 1-palmitoyl-2-oleoyl-sn-glycero-3-phosphoethanolamine (POPE) and 1-palmitoyl-2-oleoyl-sn-glycero-3-phospho-1'-rac-glycerol (POPG)[54-56] (Figure 1). These solvent stressors were chosen because THF is an effective biomass pretreatment solvent[13, 15, 16, 57-60], while butanol serves as both a pretreatment solvent and a microbial fermentation product[61-65]. By understanding the molecular interactions that drive membrane disruption by these solvents, the results of this study will provide key insights for future rational microbial engineering campaigns by revealing the different membrane solvent interactions that drive bilayer disruption.

## Methods

*Sample Preparation*

1-palmitoyl-2-oleoyl-sn-glycero-3-phosphoethanolamine (POPE) and 1-palmitoyl-2-oleoyl-sn-glycero-3-phospho-(1'-rac-glycerol) (POPG), in powder form, were supplied by Avanti Lipids (Alabaster, AL). Deuterium oxide (99.96% pure) was obtained from Cambridge Isotope Laboratories (Andover, MA). Lipid films were prepared by solubilizing, in chloroform, POPE, and POPG at a 3:1 mole fraction, approximating an inner bacterial membrane[55], and then evaporating the solvent under a stream of $N_2$ gas for 30 minutes, followed by drying under vacuum overnight to remove any trace amounts of chloroform. Multilamellar vesicles (MLVs) were prepared by warming the dried lipid film to 50°C and then hydrating in a mixture of $H_2O/D_2O$. MLVs were subjected to five freeze/thaw cycles and were then used to prepare unilamellar vesicles (ULVs) by warming the suspension to 55°C and passing it 33 times through a mini-extruder (Avanti Lipids, Alabaster, AL) assembled with a 50 nm pore-diameter polycarbonate filter (Millipore Sigma, St. Louis, MO). ULVs were then used for SAS experiments, as described below.

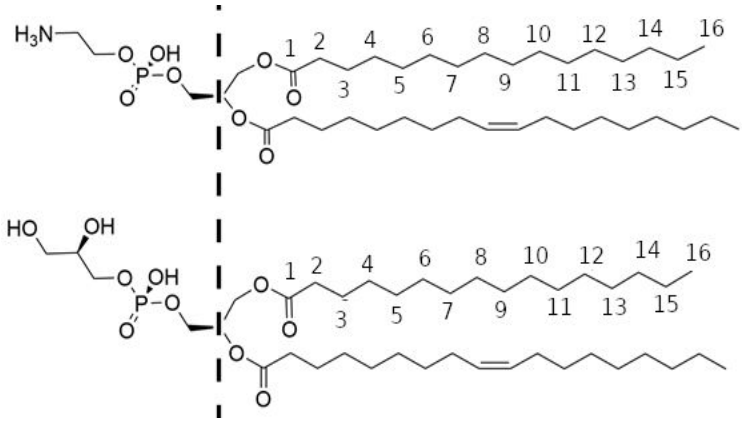


**Figure 1.** Lipid Structures. Top) 1-palmitoyl-2-oleoyl-sn phosphatidylethanolamine (POPE). Bottom.)1-palmitoyl-2-oleoyl-sn-phoshatidylglycerol (POPG). In our calculations, left of the dashed line are the so-called "head-group" atom, while those to the right are referred to as the tails.

*Small-Angle Neutron/X-Ray Scattering (SANS/SAXS)*

Small-angle neutron scattering (SANS) from ULVs composed of POPE and POPG (3:1 mole fraction) was performed on the Bio-SANS instrument located at the High-Flux Isotope Reactor facility at Oak Ridge National Laboratory[66]. ULVs were loaded into cylindrical Hellma cells of 1 mm thickness. A single instrument configuration was employed, where the main detector was positioned 15.5 m from the sample,

with a smaller "wing" detector, rotated by 1.4 °, located in close proximity to the sample. A 6 Å wavelength (λ) neutron beam was chosen with a wavelength spread (Δλ/λ) of 0.15. Neutron beam collimation was set by two circular apertures of diameters 40 mm (source) and 14 mm (sample) placed at 17.5 m apart. The processed (2D) images were corrected for detector dark current, pixel sensitivity and background scattering from the quartz cell, and normalized to the incident beam monitor counts. The processed 2D images of the sample were then azimuthally averaged to generate the one-dimensional (1D) scattering intensity profiles I(Q) versus Q.

SAXS measurements of ULVs were performed using a Rigaku (The Woodlands, TX, USA) BioSAXS2000 instrument with a copper anode X-ray source (λ~ 1.5418 Å). The instrument is configurated to produce data over a Q-range spanning from 0.01 to 0.7 $Å^{-1}$. All data were normalized and reduced using the Rigaku software package to obtain 1D scattering intensity profiles of I(Q) vs. Q. Samples were stored in a 96 well-plate sample-holder and automatically placed into the X-ray beam using a flow-cell system.

POPE:POPG ULVs at 3:1 (mole fraction) were measured at increasing concentrations of solvents: i.e., butanol (0, 1.0, 2.0 and 3.0 wt%) and THF (0, 2.0, 4.0, 6.0 wt%) in four contrast aqueous solutions, namely 100% $H_2O$, and 100%, 70% and 50% $D_2O$. Lipids concentration was 20 mg/ml. Different contrast data were simultaneously fit using a spherical core-multi-shell model with a polydisperse spherical core and hard-sphere inter-particle interactions (implemented in SASView)[67]. The spherical core represents the aqueous solution, and the three spherical shells represent the molecular structure of the POPE: POPG lipid bilayer: *i.e.,* inner bilayer leaflet head group, a common tail region for both the inner/outer leaflets, and the outer leaflet head group, where the single tail region is flanked by the inner/outer leaflet head groups of the lipid bilayer. During the fits, the only free parameters were the tail and head group thicknesses, head group scattering length density (SLD), and interparticle (vesicle) correlation distance. This model is based upon the assumptions that: (i) the SLD of the tail region is fixed at the nominal values given in Tables S1-S6 and remains unaltered from any potential partition of hydrogenated solvent; and ii) the bilayer leaflets are chemically and structurally symmetric, (layer thickness and SLD) are identical. The model is described in greater detail in the SI.

*Molecular Dynamics Simulations*

All-atom molecular dynamics (MD) studies of a model bacterial bilayer were used to obtain molecular-scale insight into the impact of THF and butanol stressors on membrane dynamics and structure. The model bacterial membrane[54-56] used consists of 60 POPG molecules and 140 POPE molecules per leaflet under aqueous environments containing varied amounts of butanol or THF (see Table 1). All force-field parameters were obtained from the CHARMM force-field family: lipids (updated additive CHARMM lipid force-field)[68], butanol (CHARMM general force-field)[69] and THF (CHARMM ether force-field)[70]. The number of atoms per system ranges from 124,006 atoms (high THF concentrations) to 124,544 atoms (no organosolv).

**Table 1.** Organic solvent/water weight ratios used in the simulations. Concentrations with a (*) correspond with concentrations used in the SAS studies. The number of organic solvent molecules in the simulations are shown in parenthesizes.

| *Butanol wt %* | *0.23 (14)* | *0.49 (29)* | *0.99* (59)* | *1.97* (117)* | *2.97* (176)* | *3.96 (243)* | *7.49 (442)* | *9.99 (586)* | *15.00 (807)* |
|---|---|---|---|---|---|---|---|---|---|
| *THF wt %* | 0.26 (16) | 0.54 (33) | 1.11* (68) | 2.16* (132) | 3.25 (198) | 4.32* (263) | 7.49 (458) | 10.01 (610) | 14.99 (908) |

The initial membrane system was constructed using a three-step process: 1) membrane generation; 2) relaxation in water; and 3) addition of aqueous organosolv. Membrane generation was facilitated using the CHARMM-GUI membrane builder.[71, 72] Energy minimization, restrained NPT relaxation, and an initial 100ns aqueous unrestrained relaxation simulation were performed using the GROMACS2016.3 simulation package[73]. Briefly, the initial, water-only solvated membrane system was energy minimized using the steepest-descent algorithm (as implemented in GROMACS) until a gradient of 1000 kJ $mol^{-1}$ $nm^{-1}$ was reached. Following energy minimization, the initial system (membrane in aqueous only-conditions) was then subjected to six subsequent NPT (P~1bar, T~303.15K) simulations, where harmonic forces restrained the lipids (as prescribed by the CHARMM-GUI), and a single production 100ns semi-isotropic NPT simulation was performed[74].

Following the relaxation in water, additional solvent boxes containing mixtures of the organic solvent (THF or butanol) with water at concentrations ranging from 0 wt% to ~15 wt% (see Table 1), were added above the membrane system (resulting in an initial box size of ~12,300,00 $Å^3$), subjected to energy minimization and six subsequent restrained semi-isotropic NPT simulations (using the same restraints previously used in the relaxation of the aqueous only system) to generate the initial geometries for production simulations. Finally, five independent per membrane-solvent mixture production simulations were performed. Each production NPT simulation was 100ns in duration, with the last 25ns of each MD trajectory used for all calculated measures. The NPT ensemble was chosen because, in contrast to NVT, it allows for the presence of membrane thinning in MD simulations. A total of 95 independent simulations (5 for each of the 19 different solvent conditions) were performed for this study.

Pressure and temperature for the production simulations were controlled by the Parrinello-Rahman and V-rescale algorithms[75-77], respectively, while the Berendsen algorithm was used to control pressure and temperature within the relaxation simulations[78]. An integration timestep of 2fs was used for the production simulations (with H-bonds constrained using the LINCS algorithm[79, 80]), while the first of the six relaxation simulations used an integration timestep of 0.1fs without constraining any bonds. The remaining relaxation simulations made use of 1fs integration timestep with bond constraints. For all simulations and energy minimization calculations, non-bonded energies were computed using standard cutoffs provided by the CHARMM-GUI generated input files, and electrostatics were calculated using the Particle Mesh Ewald formalism (PME) as implemented in GROMACS[81].

Membrane Morphology. Membrane morphology was quantified by the membrane area, transverse density profiles of the lipid headgroups and headgroup phosphate atoms, and lipid tail deuterium order parameters[82] (from C1 through C14 of the sn1 chain). The membrane area was computed as the average product of the lateral dimensions of the relaxed membrane using the gmx energy utility. Membrane thickness was derived by first computing instantaneous transverse density profiles at each frame and then extracting the locations of the two phosphate peaks (peak-to-peak) and outermost half-maximum (taken as the ‘x’ coordinates that correspond to the locations of where the leaflet distributions

are at half their maximum values) corresponding to the two bilayer leaflets. The differences in the peak-to-peak and outermost half-maximum to half-maximum distances (see Illustration S1) were used as proxies for the thickness of the membrane, with the latter used to aid comparison to SAS derived thicknesses and the former used as a traditional simulation reference point. The lipid headgroup was taken as all non-fatty acid chain atoms (see Figure 1). Head group density profiles were generated using the gmx density tool (see Organic Solvent localization for details regarding the density profile calculations). Lipid tail deuterium order parameters[83] (from C1 to C14 of the saturated chain) were computed using the gmx order tool. It is important to note that the membranes were simulated such that they were free to thin during the simulation – *i.e.,* the simulations contain no experimentally-derived constraints on the area-per-lipid. As such, it is expected that the simulations will provide a detailed but qualitative (or at best semi-quantitative) picture of membrane behavior under solvent stress – quantitative details are beyond the reach of simulations with current force-fields[68, 84].

Membrane Dynamics (Fluidity). Membrane dynamics were quantified by the computation of the lateral diffusion constants of the lipid head-group phosphate groups and the bending moduli of the membrane. The lateral diffusion constants were obtained by calculating the average mean-squared-displacement of the phosphorus atoms of the lipid head-groups as a function of time, and fitting the profile (using the standard Einstein relation: $\langle \Delta\vec{x}(t)^2 \rangle = 4Dt$ , where $D$ is the diffusion constant, and the factor of 4 replaces the standard 6 as the diffusion of interest is purely lateral, i.e., two-dimensional). The calculation of the diffusion constants and mean-squared displacements were performed using the gmx msd tool in the GROMACS simulation package. Membrane bending moduli were obtained using a set of in-house VMD[85] and Python analysis scripts (available by request) that compute the splay and tilt of the lipid components and take advantage of the relationship between these measures and the bending moduli, as described in Khelashvili et al[86].

Organic Solvent Localization. The average location of the organic solvent molecules was quantified by constructing symmetrized 1D number density profiles of the organic solvent components

along the transverse axis (z-dimension) of the membrane relative to its center. The profiles were obtained using the gmx density tool with 200 bins.

Hydrogen-Bonds. Hydrogen-bonds were calculated using gmx hbond with distance and angle cutoffs of 3Å and 20°.

**Results**

*Small-Angle Scattering*

Lipid vesicles (3:1 POPE and POPG mole fraction) were studied using small-angle neutron and X-ray scattering with varying concentrations of butanol and THF. The SAXS and SANS data are complementary, with neutrons being highly sensitive to lighter elements, such as hydrogen, while X-rays are sensitive to the electron-rich regions. Thus, neutrons, due to their high sensitivity to the carbonyl moieties, can be used to define a bilayer acyl chain (tail) thickness in terms of the distance between the carbonyl moieties of the two leaflets. In contrast, X-rays are sensitive to the phosphate groups and, therefore, can be used to estimate the total bilayer thickness. Combining SAXS data with SANS data (at three different contrasts, *i.e.* 100%, 70%, and 50% $D_2O$), the overall bilayer thickness and the tail thickness can be estimated.

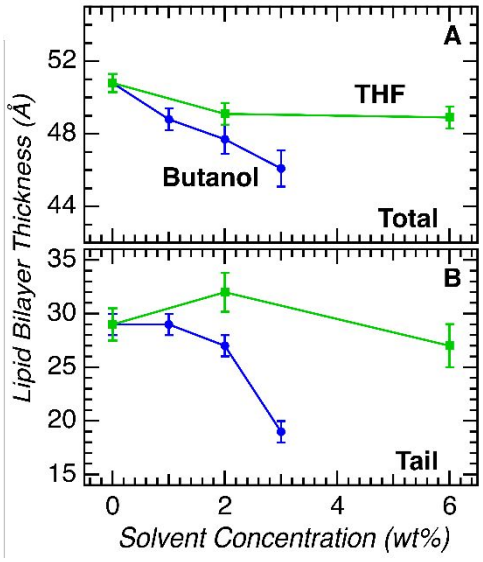


**Figure 2**. Lipid bilayer thickness determined by SAXS/SANS analysis as a function of butanol (blue dots/line) and THF (green squares/lines). (A) total bilayer thickness and (B) central acyl chain hydrophobic thickness. Solid lines are guides to the eye.

Fitting of scattering profiles for each sample was accomplished using a spherical core-multi-shell model with a polydisperse spherical core and hard-sphere interactions. The model fitting was used to obtain the set of specific structural parameters from optimal contrast conditions namely,

- 100% $D_2O$ SANS provides constraints on the overall vesicle radius, radial polydispersity, and the interparticle correlation distance from the low-*Q* data
- 100% $H_2O$ SAXS gives rise to an estimate of the overall bilayer thickness
- 50% $D_2O$ SANS provides data necessary to determine acyl chain thickness

The resulting parameters from the model are listed in Tables S1-S6 (see SI), and the fits are shown in Figures S1 and S2.

Two important bilayer features obtained from the experimental analysis, the total bilayer thickness, and the lipid acyl tail thickness, are shown in Figure 2. The total bilayer thickness (Figure 2A) decreases nearly monotonically with increasing butanol concentration, while similar, albeit smaller, thinning is also found with the addition of THF (with the 2 wt% THF and 6 wt% samples within statistical error). Direct comparison of butanol at 3 wt% with THF at 4% shows that, at similar concentrations (3% butanol vs. 4% THF), butanol has twice the thinning effect (by ~9% compared to ~4%) of THF. Moreover, butanol also leads to significant thinning of the bilayer tail region, while thinning of the tails is not statistically significant for the THF concentrations considered. To interpret the trend in membrane thickness variation as a function of solvent concentration, more solvent concentrations are needed.

*Computational Results*

Membrane Morphology and Dynamics.

Simulations provide a wealth of information about the different ways that butanol and THF impact the membrane beyond the structural changes available from scattering. Key amongst this information are specific molecular details of lipid order parameters, solvent lipid interactions such as changes in the hydrogen bond pairs, diffusion coefficients, and bending moduli. The simulations were validated by calculating the absolute (Figure 3) and relative (Figure 4) thinning of the bilayer at different solvent concentrations and comparing the simulation results to those obtained from the SAS experimental data. Figure 3 shows that as a function of increasing organic solvent concentration, the membrane

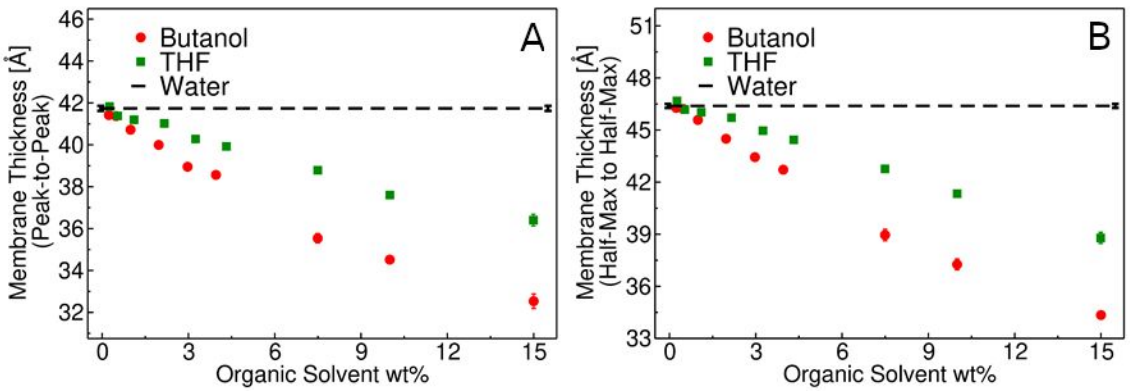


**Figure 3**. Total membrane thickness obtained from the density profiles of the phosphate atoms in the simulations. A) Derived from Peak-to-Peak distances. B) Derived from outermost Half-Max to Half-Max distances. A direct comparision of absolute values for the half-max to half-max distances is provided in figure S3. See Illustration S1 for a grapical defination of the Peak-to-Peak and Half-Max to Half-Max

thickness decreases (*i.e.* the leaflet-leaflet head-group distances decrease, see Illustration S1). An associated increase in area per lipid is also observed when the bilayer is exposed to either butanol or THF, with butanol having a larger effect (Figure S4). Direct comparisons between the absolute membrane thickness obtained from simulation and experiment (Figure S3) do indicate that the computational membranes are systematically thinner, which can result from the inaccuracy of the model used, both in the simulations (force-field accuracy and/or the use of periodic boundary conditions) and/or in the interpretation of the experiments (vesicle effects and/or assumptions and errors involved in the experimental fits). The accuracy of the simulations could be improved by optimizing the force field used. However, and more importantly, the percent change in bilayer thickness calculated from the simulations is similar to that derived from the small-angle experiments (Figure 4). In addition to the comparisons to experiment shown in Figures 3, 4, S3, S4, and S5, the density profiles of the tails were also computed, and we find a thinning of the tails in both simulations and experiments (Figure S6).

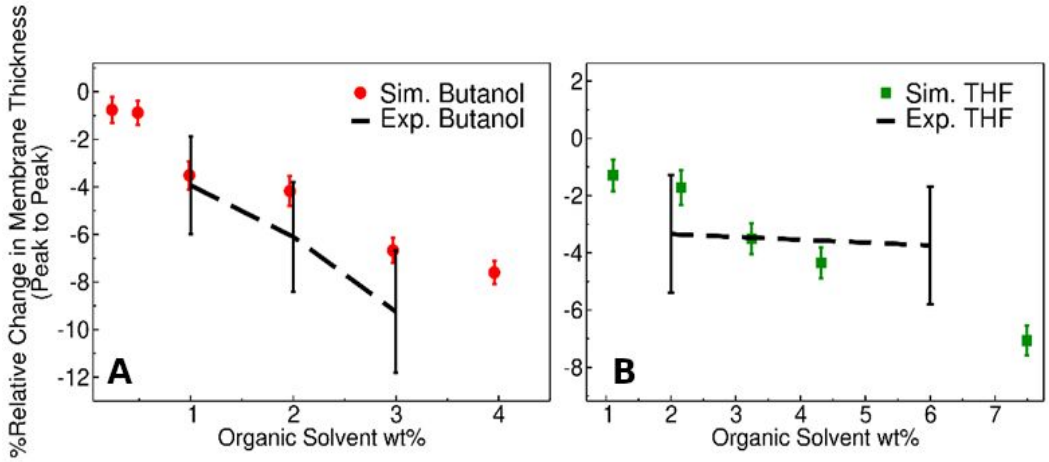


**Figure 4.** Comparison of the experiment and simulation (Peak-to-Peak, Illustration S1) determined fractional relative change in the overall membrane thickness as a function of (A) Butanol and (B) THF in the POPE:POPG (3:1) lipid bilayer system. We report percentage differences.

Both the experimental and computational data clearly show that the presence of cosolvents thins the

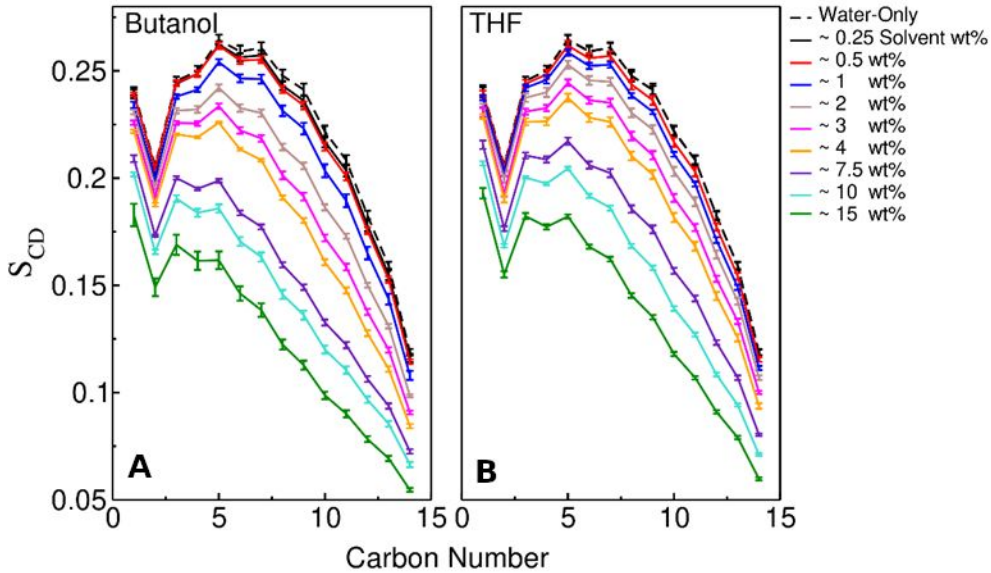


**Figure 5**. Deuterium Lipid order parameters[81] (Error bars are standard error of the mean). (A) Order parameters under butanol stress. (B) Order parameters under THF stress.

bilayer, typically a sign of increased chain disorder[87]. Further, structural measures of the acyl chain/tail thickness (Figures 2B and S5) suggest that butanol may disorder the tails more than THF. A quantitative description of the chain disorder is obtained from MD derived carbon-deuterium order parameters, $S_{CD}$

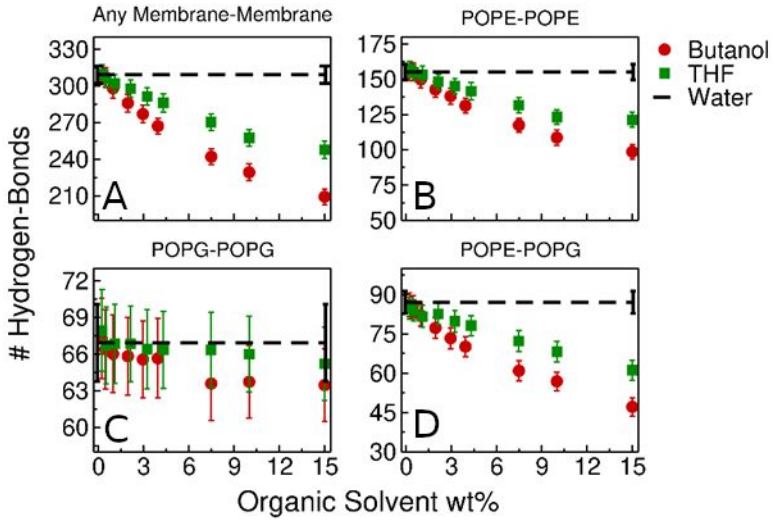


**Figure 6.** Lipid-Lipid hydrogen-bonding. A) All membrane-membrane hydrogen-bonds. B) Hydrogen-bonds between POPE molecules. C) Hydrogen-bonds between POPG molecules. D) Hyrdrogen-bonds between POPG and POPE. Error-bars are standard error of the mean. Dashed-lines represent hydrogen-bonding values in the absence of cosolvents.

(Figure 5), which clearly shows that lipid order decreases upon cosolvent addition in a concentration-dependent fashion. Furthermore, butanol has a greater disordering effect than THF, particularly for carbons 1-6 (closer to the head-group). It should be noted, however, that the disordering effect on the terminal carbon at the midplane of the bilayer does not show a substantial change in order until ~1% butanol or ~3% THF.

Lipid structure is tightly correlated to the intermolecular hydrogen bonding of the lipids comprising the bilayer[88]. Figure 6 illustrates the significant reduction of lipid-lipid hydrogen bonding as cosolvent concentrations increase. For example, PE (phosphatidylethanolamine) lipids frequently have higher melting temperatures, relative to PC lipids, due in part to the increased propensity to hydrogen bond with neighboring molecules[89, 90]. The presence of butanol or THF cosolvents disrupts these headgroup interactions. PG-PG interactions are found to be the least impacted by the presence of cosolvents. Butanol again shows the more substantial effect, disrupting ~30% of the total hydrogen bonds (Fig. 6, upper left) in the bilayer at 15 wt%. Further, it is interesting to note that comparing the trends in Fig. 6 with those shown in Fig. S4 shows a close agreement between bilayer area expansion and the reduction of lipid-lipid hydrogen bonds.

Membrane fluidity and mechanical stability are crucial to biological function and membrane organization[91-94]. These parameters are closely associated with the structure of the bilayer and will be impacted by the observed bilayer thinning and area expansion. To gauge the impact of THF and butanol on the dynamics and mechanics of the membrane, both the lateral diffusion of the phosphate atoms from the lipid head-groups (Figure 7) and the bending moduli of the membrane (Figure 8) were computed – the diffusion coefficient is inversely related to the membrane viscosity[95]. Here, with the addition of ~1% of

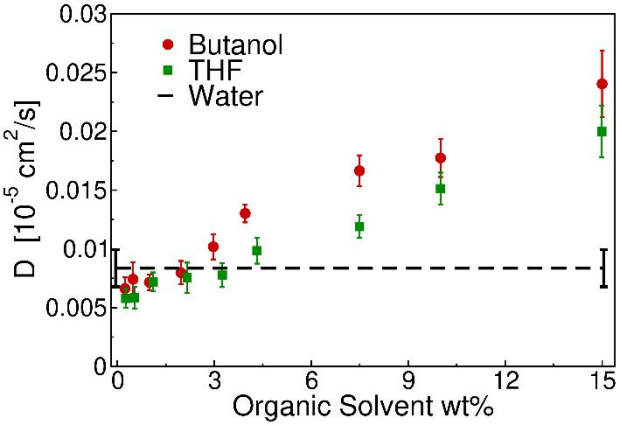


**Figure 7.** Apparent (linear regime-approximation, see Figure S7 for mean-square displacement plots used for the determination of these constants) lateral diffusion constant. Error-bars are standard errors derived from the fits of five different indepent simulations per concentration. Dashed lines reprsent simulations in water.

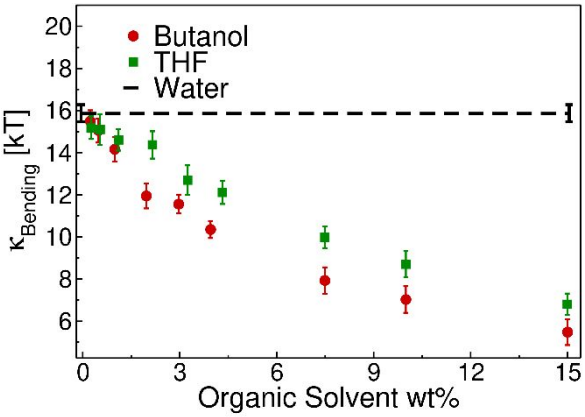


**Figure 8.** Bending moduil derived from lipid-splay[84]. Error-bars are standard errors of the mean. Dashed lines represent simulations in water.

cosolvent (butanol or THF), a small (within overlapping error-bars of the aqueous control) drop can be seen denoting a small increase in viscosity for both solvents, before decreasing in a concentration-dependent fashion. The changes to both the diffusion coefficient and the bending modulus are consistent with the previously noted changes in morphology (Figures 1-6 and S1-6), with butanol having a larger impact than THF.

Solvent Localization and Solvent-Membrane Interactions.

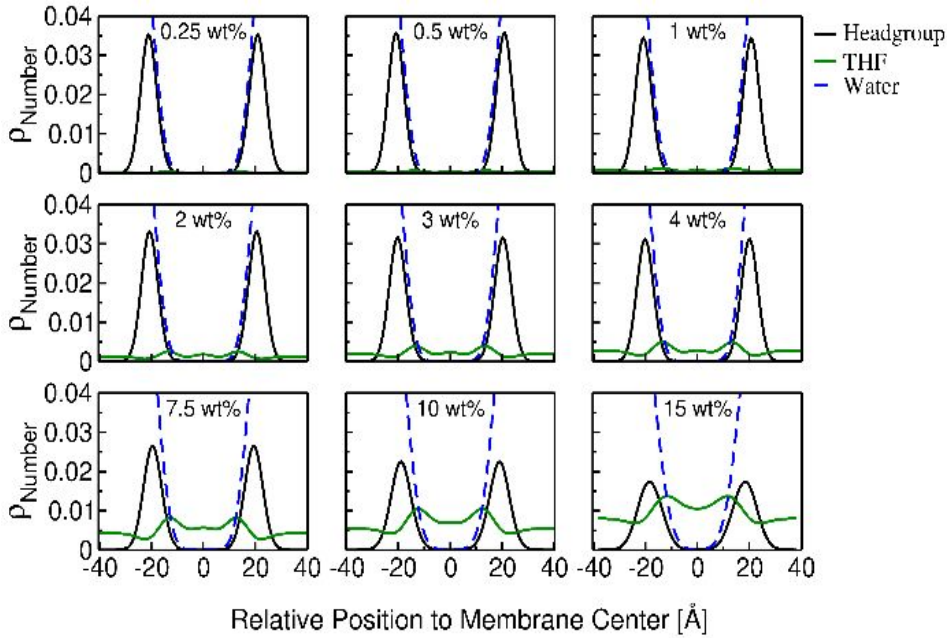


**Figure 9**. THF and water solvent density profiles. Solid black curves represent the position of the membrane head-groups.

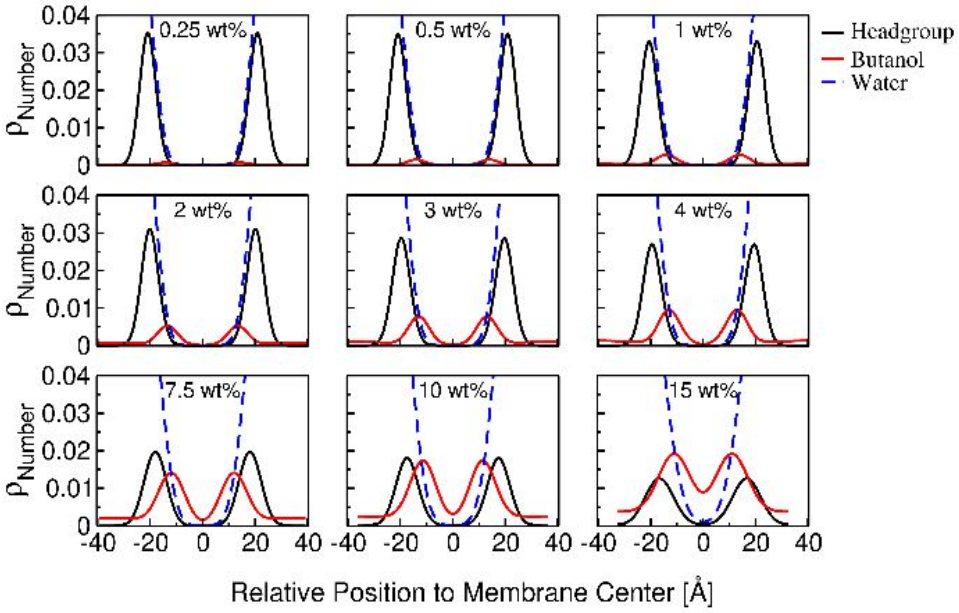


**Figure 10.** Butanol and water solvent density profiles. Solid black curves represent the position of the center-of-mass of the lipid head-groups

It is also of interest to track the location of the solvent components relative to the membrane with the aim

of understanding how cosolvent localization may be related to the observed changes. To this end, 1D density profiles were computed (Figures 9 and 10) for the headgroup centers of mass for both butanol and THF. Further, by integrating the curves in Figures 9 and 10 from -20 to 20Å, the amount of incorporation of each organic solvent can be estimated. The total amount of THF incorporated into the membrane ranges from 7% to 20% (mol%) as a function of increasing concentration, while ~25% to ~50% of butanol incorporates into the membrane in a similar concentration-dependent manner. Taking the incorporation values and the total box volumes allow for an estimate of the partition coefficients (log $P_{memb/aqueous}$, with log $P_{memb/aqueous} = \rho_{memb}/\rho_{aq}$, where subscript $\rho_{memb}$ corresponds to the local organic solvent density within the membrane, with a fixed thickness of 40 Å, to correspond with the integration performed, and $\rho_{aq}$ is the organic solvent density within the aqueous phase) for THF and butanol. As a function of increasing concentration, THF is found to have a partition coefficient ranging from 0.166 (at low concentration) to 0.177 (at high concentration), while butanol has a partition coefficient of 0.88 (at low concentration) to 0.52 (at high concentration).

In addition to the quantification of organic solvent incorporation, Figures 10 and 11 also indicate that organic solvent density in the bilayer appears to be focused at both the glycerol/carboxyl region (where water and lipid hydrogen bonding partners are accessible) and the hydrophobic tail region. Interestingly, butanol incorporation is primarily found at the lipid head group/tail interface, near the glycerol/carboxyl region, though at high butanol concentrations (i.e. >7.5%) the solvent does begin to be observed near the bilayer midplane. THF, on the other hand, is found at both the head-group and deep within the tail region of the membrane, even at low THF concentrations, suggesting a fundamentally different interaction with the lipids than butanol – one that may not favor THF-lipid head interactions, but instead, favors THF-lipid tail interactions (limits THF from transiting the head-group domain of the membrane).

Hydrogen-bonding between the lipids was shown to decrease significantly (Figure 6). With the loss of the inter-lipid hydrogen bonds (HBs), we now evaluate the development of new solvent – lipid and water-lipid HBs, shown in Figure 11. There is a clear difference in the absolute number of lipid-organic solvent HBs between the two cosolvents, with butanol creating substantially more HBs with the lipids than THF. This disparity in the absolute number of lipid-organic solvent HBs is likely due, in part, to the ability of butanol to serve as both a hydrogen-bond donor or acceptor[96], while THF can only accept hydrogen bonds[97].

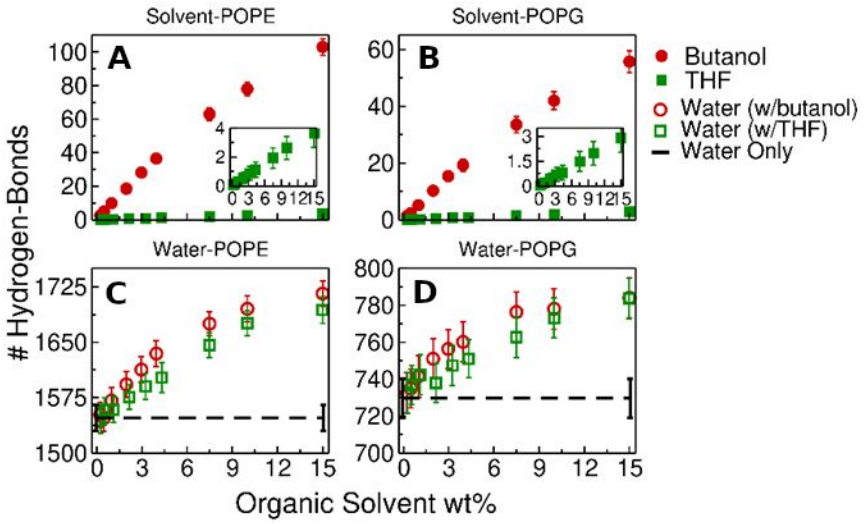


**Figure 11.** Solvent-Lipid hydrogen-bonds. Error-bars are standard error of the mean. The dashed line provided as a comparison to the same membrane under aqeous conditions. (A) Hydrogen-bonds between the organic solvents and POPE. (B) Hydrogen-bonds between the organic solvents and POPG. (C) Hydrogen-bonds between water and POPE. (D) Hydrogen-bonds between water and POPG. Open shape (green squares and red circles) in (C) and (D) denote whether the water hydrogen-bonds occur in simulaitons with butanol or THF.

Comparing the impact of the organic solvents on water-membrane interactions (bottom two panels of Figure 11) indicates that the presence of THF or butanol does increase these interactions with comparable magnitudes. Given the similarities between the water-lipid interactions and differences between the organic solvent-lipid interactions, this suggests that although both increase water-lipid interactions, the mechanisms driving these increases are fundamentally different between the two solvents.

**Discussion.**

Microbial membranes have long been known to be disrupted by organic solvents [24, 98-101]. However, molecular studies of the impacts of organic solvents (other than ethanol) on biomembrane morphology and dynamics have been limited in the literature[24, 98-101]. The combined experimental and theoretical work presented here provides a molecular-scale view of the morphological changes taking place in a microbial membrane model under increasing THF or butanol stress. The extent of these changes is quite different between the two solvents, indicating fundamentally different disruption mechanisms. Importantly, there is a consistency between experiments and simulation results (Figure 4) regarding the total bilayer thickness as a result of the stress induced by the organic solvents (THF and butanol).

Butanol is a prototypical amphiphilic alcohol and localizes near the head-tail interface. Both membrane-membrane and membrane-water hydrogen-bonds are altered, with membrane-solvent hydrogen-bonds substituting for membrane-membrane hydrogen-bonds (Figures 6 and 11). By partitioning into the head-tail interface (Figure 10), butanol expands the membrane area (Figure S4), forcing the hydrophobic region of the lipid to "crumple" (Figure 5) in order to avoid water penetration into the membrane center, as more water forms hydrogen-bonds with the lipid heads (Figure 11).

THF incorporation into the membrane is limited, in comparison to butanol (Figure 9), with a significant portion (80-93% of all THF) remaining outside of the membrane at all concentrations, in contrast to butanol, which readily incorporates into the membrane (with 25% to 50% found within the membrane). In contrast to butanol, THF can only accept hydrogen-bonds, limiting its ability to make favorable hydrogen-bonding interactions with the lipid near the hydrophilic/hydrophobic interface. As such, THF does not form an extensive hydrogen-bonds with the lipid heads but rather penetrates deeper into the membrane bilayers, partitioning into the acyl tail of the bilayer. By partitioning into the hydrophobic tail and not forming hydrogen bonds at the head-tail interface, the tails must disorder to accommodate THF, which in turn forces the bilayer to expand and thin. Upon expansion, water-lipid interactions are enhanced by THF. As THF does not directly disrupt water-lipid interactions but instead

introduces stress into the tails, lipid-lipid hydrogen-bonding is less disrupted, providing some stabilization to the membrane. As a consequence, membrane fluidization under THF stress is limited when compared to fluidization resulting from similar concentrations of butanol.

**Conclusions**

Preventing the disruption of microbial membrane homeostasis under fermentation and residual pretreatment organic solvent stress is of critical importance in order to increase the cost-effectiveness of lignocellulosic biofuels and bioproducts. By using a combination of small-angle scattering and molecular simulations, this work provides molecular-scale insights into the impacts of two common organic solvents on model microbial membranes. The results presented indicate that disruption of the head-tail interface is a strong driver of membrane-thinning and membrane fluidization as a result of butanol or THF stresses. Amphiphilic molecules, such as butanol, capable of hydrogen bonding with adjacent lipids, may have a more profound effect than molecules such as THF, which expand the bilayer area by inserting themselves into the membrane hydrophobic core but do not directly hydrogen bond to the membrane lipids. This suggests that targeted engineering of the lipid head-fatty acid tail interface may be solvent dependent and require a rational approach to enhance microbial resistance to fermentation and bioprocessing stresses.

**Acknowledgments**

This research was supported by the Genomic Science Program, Office of Biological and Environmental Research, U. S. Department of Energy (DOE), under Contract FWP ERKP752. This research used resources of the Compute and Data Environment for Science (CADES) at the Oak Ridge National Laboratory, which is supported by the Office of Science of DOE, and of the National Energy Research Scientific Computing Center (NERSC), a DOE Office of Science User Facility operated under Contract No. DE-AC02-05CH11231. Neutron scattering research conducted at the Bio-SANS instrument, a DOE Office of Science, Office of Biological and Environmental Research resource, used resources at the High Flux Isotope Reactor, a DOE Office of Science, Scientific User Facility operated by the Oak Ridge

National Laboratory. Oak Ridge National Laboratory is managed by UT-Battelle, LLC, for the U. S. Department of Energy under Contract DE-AC05-00OR22725.

**Conflict of Interest.**

The authors report that there are no conflicts to declare

**References**


1. M. E. Himmel, *Biomass recalcitrance : deconstructing the plant cell wall for bioenergy*, Blackwell Pub., Oxford, 2008.
2. X. Zhao, L. Zhang and D. Liu, *Biofuels, Bioproducts and Biorefining*, 2012, **6**, 465-482.
3. X. B. Zhao, L. H. Zhang and D. H. Liu, *Biofuel Bioprod Bior*, 2012, **6**, 561-579.
4. A. Q. Zheng, Z. L. Zhao, Z. Huang, K. Zhao, G. Q. Wei, L. Q. Jiang, X. B. Wang, F. He and H. B. Li, *Green Chem*, 2015, **17**, 1167-1175.
5. C. Carmona, P. Langan, J. C. Smith and L. Petridis, *Phys Chem Chem Phys*, 2015, **17**, 358-364.
6. M. D. Smith, in *Understanding Lignocellulose: Synergistic Computational and Analytic Methods*, American Chemical Society, 2019, vol. 1338, ch. 1, pp. 1-15.
7. B. Yang and C. E. Wyman, *Biofuels, Bioproducts and Biorefining: Innovation for a sustainable economy*, 2008, **2**, 26-40.
8. R. Kumar, S. Bhagia, M. D. Smith, L. Petridis, R. G. Ong, C. M. Cai, A. Mittal, M. H. Himmel, V. Balan, B. E. Dale, A. J. Ragauskas, J. C. Smith and C. E. Wyman, *Green Chem*, 2018, **20**, 921-934.
9. H. Teramura, K. Sasaki, T. Oshima, F. Matsuda, M. Okamoto, T. Shirai, H. Kawaguchi, C. Ogino, K. Hirano, T. Sazuka, H. Kitano, J. Kikuchi and A. Kondo, *Biotechnol Biofuels*, 2016, **9**.
10. R. Sindhu, P. Binod, K. U. Janu, R. K. Sukumaran and A. Pandey, *World Journal of Microbiology and Biotechnology*, 2012, **28**, 473-483.
11. M. A. Mellmer, D. M. Alonso, J. S. Luterbacher, J. M. R. Gallo and J. A. Dumesic, *Green Chem*, 2014, **16**, 4659-4662.
12. M. A. Mellmer, C. Sener, J. M. R. Gallo, J. S. Luterbacher, D. M. Alonso and J. A. Dumesic, *Angew Chem Int Edit*, 2014, **53**, 11872-11875.
13. M. D. Smith, B. Mostofian, X. Cheng, L. Petridis, C. M. Cai, C. E. Wyman and J. C. Smith, *Green Chem*, 2016, **18**, 1268-1277.
14. M. D. Smith, L. Petridis, X. Cheng, B. Mostofian and J. C. Smith, *Phys Chem Chem Phys*, 2016, **18**.
15. B. Mostofian, C. M. Cai, M. D. Smith, L. Petridis, X. Cheng, C. E. Wyman and J. C. Smith, *J Am Chem Soc*, 2016.
16. M. D. Smith, C. M. Cai, X. Cheng, L. Petridis and J. C. Smith, *Green Chem*, 2018, **20**, 1612-1620.
17. M. D. Smith, X. Cheng, L. Petridis, B. Mostofian and J. C. Smith, *Sci Rep-Uk*, 2017, **7**, 14494.
18. A. S. Patri, B. Mostofian, Y. Pu, N. Ciaffone, M. Soliman, M. D. Smith, R. Kumar, X. Cheng, C. E. Wyman, L. Tetard, A. J. Ragauskas, J. C. Smith, L. Petridis and C. M. Cai, *J Am Chem Soc*, 2019, **141**, 12545-12557.
19. S. V. Pingali, M. D. Smith, S.-H. Liu, T. B. Rawal, Y. Pu, R. Shah, B. R. Evans, V. S. Urban, B. H. Davison, C. M. Cai, A. J. Ragauskas, H. M. O'Neill, J. C. Smith and L. Petridis, *Proceedings of the National Academy of Sciences*, 2020, **117**, 16776-16781.
20. C. G. Yoo, X. Meng, Y. Pu and A. J. Ragauskas, *Bioresource Technology*, 2020, **301**, 122784.
21. N. A. Buijs, V. Siewers and J. Nielsen, *Current opinion in chemical biology*, 2013, **17**, 480-488.

22. L. Caspeta, N. A. A. Buijs and J. Nielsen, *Energ Environ Sci*, 2013, **6**, 1077-1082.
23. J. A. Cray, A. Stevenson, P. Ball, S. B. Bankar, E. C. A. Eleutherio, T. C. Ezeji, R. S. Singhal, J. M. Thevelein, D. J. Timson and J. E. Hallsworth, *Current Opinion in Biotechnology*, 2015, **33**, 228-259.
24. H. J. Heipieper, F. J. Weber, J. Sikkema, H. Keweloh and J. A. M. de Bont, *Trends Biotechnol*, 1994, **12**, 409-415.
25. A. Mukhopadhyay, *Trends in Microbiology*, 2015, **23**, 498-508.
26. E. Lamsen and S. Atsumi, *Frontiers in Microbiology*, 2012, **3**.
27. H. B. Klinke, A. B. Thomsen and B. K. Ahring, *Appl Microbiol Biot*, 2004, **66**, 10-26.
28. X. Wang, L. P. Yomano, J. Y. Lee, S. W. York, H. Zheng, M. T. Mullinnix, K. T. Shanmugam and L. O. Ingram, *Proceedings of the National Academy of Sciences*, 2013, **110**, 4021.
29. P. T. Pienkos and M. Zhang, *Cellulose*, 2009, **16**, 743-762.
30. L. D. Gottumukkala, K. Haigh and J. Görgens, *Renewable and Sustainable Energy Reviews*, 2017, **76**, 963-973.
31. K. Ullah, V. K. Sharma, M. Ahmad, P. Lv, J. Krahl, Z. Wang and Sofia, *Renewable and Sustainable Energy Reviews*, 2018, **82**, 3992-4008.
32. T. W. Jeffries and Y.-S. Jin, in *Advances in Applied Microbiology*, Academic Press, 2000, vol. 47, pp. 221-268.
33. L. J. Jönsson and C. Martín, *Bioresource Technol*, 2016, **199**, 103-112.
34. N. Banerjee, R. Bhatnagar and L. Viswanathan, *European journal of applied microbiology and biotechnology*, 1981, **11**, 226-228.
35. R. J. Conrado, J. D. Varner and M. P. DeLisa, *Current opinion in biotechnology*, 2008, **19**, 492-499.
36. B. Alberts, A. Johnson, J. Lewis, D. Morgan, M. Raff, K. Roberts and P. Walter, *NY: Garland Science*, 2016.
37. C. Hannesschlaeger, A. Horner and P. Pohl, *Chemical Reviews*, 2019, DOI: 10.1021/acs.chemrev.8b00560.
38. X. Cheng and J. C. Smith, *Chemical Reviews*, 2019, DOI: 10.1021/acs.chemrev.8b00439.
39. A. B. Duncan, S. Fellous, E. Quillery and O. Kaltz, *Res Microbiol*, 2011, **162**, 939-944.
40. A. Zhou, E. Baidoo, Z. He, A. Mukhopadhyay, J. K. Baumohl, P. Benke, M. P. Joachimiak, M. Xie, R. Song and A. P. Arkin, *The ISME journal*, 2013, **7**, 1790.
41. K. M. Dombek and L. Ingram, *J Bacteriol*, 1984, **157**, 233-239.
42. J. E. Cronan Jr and E. P. Gelmann, *Bacteriological reviews*, 1975, **39**, 232.
43. J. Beranová, M. Jemioła-Rzemińska, D. Elhottová, K. Strzałka and I. Konopásek, *Biochimica et Biophysica Acta (BBA)-Biomembranes*, 2008, **1778**, 445-453.
44. J. D. Nickels, M. D. Smith, R. J. Alsop, S. Himbert, A. Yahya, D. Cordner, P. Zolnierczuk, C. B. Stanley, J. Katsaras and X. Cheng, *The Journal of Physical Chemistry B*, 2019.
45. S. H. Baer, H. P. Blaschek and T. L. Smith, *Appl Environ Microb*, 1987, **53**, 2854-2861.
46. W. Hugo, *Microbios*, 1978, **23**, 83-85.
47. J. Sikkema, B. Poolman, W. N. Konings and J. De Bont, *J Bacteriol*, 1992, **174**, 2986-2992.
48. J. Sikkema, J. A. M. Debont and B. Poolman, *Microbiol Rev*, 1995, **59**, 201-222.
49. H. J. Heipieper, F. J. Weber, J. Sikkema, H. Keweloh and J. A. M. Debont, *Trends Biotechnol*, 1994, **12**, 409-415.
50. J. Sikkema, J. A. M. Debont and B. Poolman, *J Biol Chem*, 1994, **269**, 8022-8028.
51. J. Sikkema, F. J. Weber, H. J. Heipieper and J. A. M. Debont, *Biocatalysis*, 1994, **10**, 113-122.
52. K. M. Docherty and C. F. Kulpa, *Green Chem*, 2005, **7**, 185-189.
53. H. V. Ly and M. L. Longo, *Biophys J*, 2004, **87**, 1013-1033.
54. W. Zhao, T. Rog, A. A. Gurtovenko, I. Vattulainen and M. Karttunen, *Biochimie*, 2008, **90**, 930-938.

55. K. Murzyn, T. Róg and M. Pasenkiewicz-Gierula, *Biophys J*, 2005, **88**, 1091-1103.
56. P. Wydro and K. Witkowska, *Colloids and Surfaces B: Biointerfaces*, 2009, **72**, 32-39.
57. T. Y. Nguyen, C. M. Cai, R. Kumar and C. E. Wyman, *Chemsuschem*, 2015, **8**, 1716-1725.
58. C. M. Cai, N. Nagane, R. Kumar and C. E. Wyman, *Green Chem*, 2014, **16**, 3819-3829.
59. C. M. Cai, T. Y. Zhang, R. Kumar and C. E. Wyman, *J Chem Technol Biot*, 2014, **89**, 2-10.
60. C. M. Cai, T. Y. Zhang, R. Kumar and C. E. Wyman, *Green Chem*, 2013, **15**, 3140-3145.
61. N. Hausser, S. Marinkovic and B. Estrine, *Cellulose*, 2013, **20**, 2179-2184.
62. M. Yang, S. Kuittinen, J. Zhang, J. Vepsalainen, M. Keinanen and A. Pappinen, *Bioresour Technol*, 2015, **179**, 128-135.
63. H. Amiri, K. Karimi and H. Zilouei, *Bioresource Technol*, 2014, **152**, 450-456.
64. S. Nanda, A. K. Dalai and J. A. Kozinski, *Energy Science & Engineering*, 2014, **2**, 138-148.
65. B. Schiel-Bengelsdorf, J. Montoya, S. Linder and P. Dürre, *Environ Technol*, 2013, **34**, 1691-1710.
66. W. T. Heller, V. S. Urban, G. W. Lynn, K. L. Weiss, H. M. O'Neill, S. V. Pingali, S. Qian, K. C. Littrell, Y. B. Melnichenko and M. V. Buchanan, *Journal of Applied Crystallography*, 2014, **47**, 1238-1246.
67. P. Butler, G. Alina, R. Hernandez, M. Doucet, A. Jackson, P. Kienzle, S. Kline and J. Zhou, *There is no corresponding record for this reference.[Google Scholar]*, 2013.
68. J. B. Klauda, R. M. Venable, J. A. Freites, J. W. O'Connor, D. J. Tobias, C. Mondragon-Ramirez, I. Vorobyov, A. D. MacKerell Jr and R. W. Pastor, *The journal of physical chemistry B*, 2010, **114**, 7830-7843.
69. K. Vanommeslaeghe, E. Hatcher, C. Acharya, S. Kundu, S. Zhong, J. Shim, E. Darian, O. Guvench, P. Lopes, I. Vorobyov and A. D. MacKerell, *J Comput Chem*, 2010, **31**, 671-690.
70. I. Vorobyov, V. M. Anisimov, S. Greene, R. M. Venable, A. Moser, R. W. Pastor and A. D. MacKerell, *J Chem Theory Comput*, 2007, **3**, 1120-1133.
71. X. Cheng, Y. F. Qi, J. Lee, S. Jo and W. Im, *Biophys J*, 2015, **108**, 159a-159a.
72. S. Jo, J. B. Klauda and W. Im, *Biophys J*, 2009, **96**, 41a-41a.
73. M. J. Abraham, T. Murtola, R. Schulz, S. Páll, J. C. Smith, B. Hess and E. Lindahl, *SoftwareX*, 2015, **1–2**, 19-25.
74. S. Jo, T. Kim and W. Im, *Plos One*, 2007, **2**, e880.
75. G. Bussi, D. Donadio and M. Parrinello, *J Chem Phys*, 2007, **126**.
76. G. Bussi, T. Zykova-Timan and M. Parrinello, *J Chem Phys*, 2009, **130**.
77. M. Parrinello and A. Rahman, *J Appl Phys*, 1981, **52**, 7182-7190.
78. H. J. C. Berendsen, J. P. M. Postma, W. F. Vangunsteren, A. Dinola and J. R. Haak, *J Chem Phys*, 1984, **81**, 3684-3690.
79. B. Hess, H. Bekker, H. J. C. Berendsen and J. G. E. M. Fraaije, *J Comput Chem*, 1997, **18**, 1463-1472.
80. B. Hess, *J Chem Theory Comput*, 2008, **4**, 116-122.
81. M. J. Abraham and J. E. Gready, *J Comput Chem*, 2011, **32**, 2031-2040.
82. A. Seelig and J. Seelig, *Biochemistry-Us*, 1974, **13**, 4839-4845.
83. L. S. Vermeer, B. L. De Groot, V. Réat, A. Milon and J. Czaplicki, *European Biophysics Journal*, 2007, **36**, 919-931.
84. N. Kučerka, B. van Oosten, J. Pan, F. A. Heberle, T. A. Harroun and J. Katsaras, *The journal of physical chemistry B*, 2014, **119**, 1947-1956.
85. W. Humphrey, A. Dalke and K. Schulten, *J Mol Graph*, 1996, **14**, 33-38, 27-38.
86. G. Khelashvili, B. Kollmitzer, P. Heftberger, G. Pabst and D. Harries, *J Chem Theory Comput*, 2013, **9**, 3866-3871.
87. T. T. Mills, G. E. S. Toombes, S. Tristram-Nagle, D.-M. Smilgies, G. W. Feigenson and J. F. Nagle, *Biophysical journal*, 2008, **95**, 669-681.

88. J. M. Boggs, *Biochimica et Biophysica Acta (BBA) - Reviews on Biomembranes*, 1987, **906**, 353-404.
89. P. M. Brown, J. Steers, S. W. Hui, P. L. Yeagle and J. R. Silvius, *Biochemistry-Us*, 1986, **25**, 4259-4267.
90. J. R. Silvius, P. M. Brown and T. J. O'Leary, *Biochemistry-Us*, 1986, **25**, 4249-4258.
91. D. A. Los, K. S. Mironov and S. I. Allakhverdiev, *Photosynthesis research*, 2013, **116**, 489-509.
92. J. D. Nickels, X. Cheng, B. Mostofian, C. Stanley, B. Lindner, F. A. Heberle, S. Perticaroli, M. Feygenson, T. Egami and R. F. Standaert, *Journal of the American Chemical Society*, 2015, **137**, 15772-15780.
93. D. A. Los and N. Murata, *Biochimica et Biophysica Acta (BBA)-Biomembranes*, 2004, **1666**, 142-157.
94. X. Cheng and J. C. Smith, *Chemical reviews*, 2019, **119**, 5849-5880.
95. P. G. Saffman and M. Delbrück, *Proceedings of the National Academy of Sciences*, 1975, **72**, 3111-3113.
96. PubChem Compound Summary for CID 263, 1-Butanol; , https://pubchem.ncbi.nlm.nih.gov/compound/1-Butanol, (accessed 2020, Aug. 2).
97. PubChem Compound Summary for CID 8028, Tetrahydrofuran, https://pubchem.ncbi.nlm.nih.gov/compound/Tetrahydrofuran, (accessed Aug. 2, 2020).
98. Y. Gao, J. Dai, H. Peng, Y. Liu and T. Xu, *Journal of Applied Microbiology*, 2011, **110**, 472-478.
99. S. Bandyopadhyay, J. C. Shelley and M. L. Klein, *The Journal of Physical Chemistry B*, 2001, **105**, 5979-5986.
100. A. Odinokov and D. Ostroumov, *The Journal of Physical Chemistry B*, 2015, **119**, 15006-15013.
101. G. Dyrda, E. Boniewska-Bernacka, D. Man, K. Barchiewicz and R. Słota, *Molecular Biology Reports*, 2019, DOI: 10.1007/s11033-019-04782-y.